Conical magnetic structures in multiferroic $SrSc_xFe_{12-x}O_{19}$ hexaferrites derived from powder neutron diffraction

N. Qureshi,[1,*] M. D. Ruiz-Martín,[2,1] I. Puente-Orench,[1,3] M. T. Fernández-Díaz,[1] A. M. Balbashov,[4] V. Yu. Ivanov,[5] V. Skumryev,[6] and A. A. Mukhin[5]

[1]*Institut Laue-Langevin, 71 avenue des Martyrs, CS 20156, 38042 Grenoble Cedex 9, France*
[2]*Grup de Caracterització de Materials, Departament de Física i Enginyieria Nuclear, ETSEIB, Universitat Politècnica de Catalunya, Diagonal 647, E-08028 Barcelona, Spain*
[3]*Instituto de Ciencia de Materiales de Aragón, CSIC-Universidad de Zaragoza, 50009 Zaragoza, Spain*
[4]*National Research University MPEI, ul. Krasnokazarmennaya 14, Moscow 111250, Russia*
[5]*Prokhorov General Physics Institute, Russian Academy of Sciences, ul. Vavilova 38, Moscow 119991, Russia*
[6]*Institució Catalana de Recerca i Estudis Avançats (ICREA), and Departament de Física, Universitat Autónoma de Barcelona, 08193 Bellaterra, Spain*

(Received 22 December 2017; revised manuscript received 13 July 2018; published 11 September 2018)

We present a systematic powder neutron diffraction study on Sr-based M-type hexaferrites $SrSc_xFe_{12-x}O_{19}$ using high-resolution and high-flux instruments. We have derived the magnetic configurations for the compounds with $x = 1.4$, 1.6, and 1.8 at room temperature and at 2 K revealing a ferrimagnetic structure and a complex conical magnetic structure, respectively, where the latter is decomposed into the axial ferrimagnetic and the helicoidally modulated component in the hexagonal a-b plane. Our temperature- and composition-dependent investigation reveals that doping nonmagnetic Sc into this system reinforces the frustration and pushes the transition between the two ordered phases toward higher temperatures. The continuous opening of the spin cone suggests a smooth transition from an easy-axis toward an easy-plane anisotropy with decreasing temperature, which can be reinforced by increasing Sc content.

DOI: 10.1103/PhysRevB.98.094411

I. INTRODUCTION

The $SrSc_xFe_{12-x}O_{19}$ system represents the family of hexaferrites that reveal remarkable magnetoelectric properties and form a distinct family within the multiferroic materials with magnetically induced electric polarization. Over the past decade, following the report of Ref. [1], electric polarization induced by a magnetic field has been found in a number of different hexaferrites with M-, Y-, Z- (Refs. [1–5]), and U-type structure [6]. In general, the value of polarization was not very large, amounting to several tens of $\mu C/m^2$ [the maximum value of 200 $\mu C/m^2$ was found in the Y-type hexaferrite: $Ba_{0.5}Sr_{1.5}Zn_2(Fe_{1-x}Al_x)O_{22}$ for $x = 0.08$ (Ref. [7])]. In some cases (Z-type hexaferrites), the polarization could be observed even at room temperature. However, a quantitative theory describing the relationship of the electric polarization with the specific magnetic structure in various hexaferrites has not been developed so far. A common concept is applied for all types of hexaferrites: the magnetic structure is considered ferrimagnetic at sufficiently high temperatures, obtained by summing the Fe spins in various crystallographic positions in the hexagonal lattice, which form distinct building blocks characterized by a total magnetic moment that is ordered ferrimagnetically and is oriented either along the hexagonal c axis or in the basal plane. Hexaferrites of M-type shown in Fig. 1(a) consist of blocks $S = 2MeFe_2O_4$ (Me = divalent metal ion), $R = MFe_6O_{11}$ (M = Ba, Sr, ...), and similar blocks R^*, S^* rotated by 180° around the c axis [see Fig. 1(b)], while Y-type hexaferrites consist of S and $T = M_2Fe_2O_{14}$ blocks, and Z-type are composed of R, S, T blocks (see Ref. [8] and references therein). Due to the competition of exchange interactions and magnetic anisotropies, spiral or conical magnetic structures may occur at some temperatures, which can further be modified by applied magnetic field. The occurrence of electric polarization is usually explained in the framework of the inverse Dzyaloshinskii-Moriya interaction mechanism for incommensurate structures. As to the M-type hexaferrites (with general chemical formula $AFe_{12}O_{19}$, space group $P6_3/mmc$), conical magnetic structures were found by neutron diffraction studies long ago in $BaSc_xFe_{12-x}O_{19}$ for $x = 1.2$–1.8 (Ref. [9]), however an electric polarization induced by a magnetic field was observed only recently in $BaSc_{1.6}Mg_yFe_{10.4-y}O_{19}$ (Ref. [10]), where the small amount of Mg, $y \sim 0.05$, was introduced to decrease conductivity. A conical magnetic structure model was proposed [9] that suggests a collinear ordering within the magnetic R' blocks as independent structural units where the total moment direction within the blocks is declined from the hexagonal axis (note that the block definition R' corresponds to R in Refs. [9,10]). The observed period of the helicoidal structure at $T = 77$ K varies from 70 Å for $x = 1.2$ to 140 Å at $x = 1.8$, which was also accompanied by the corresponding increase of the cone vertex half-angle from 12° to 30°. These results have been confirmed by further magnetic, neutron diffraction, and

*Author to whom all correspondence should be addressed: qureshi@ill.fr

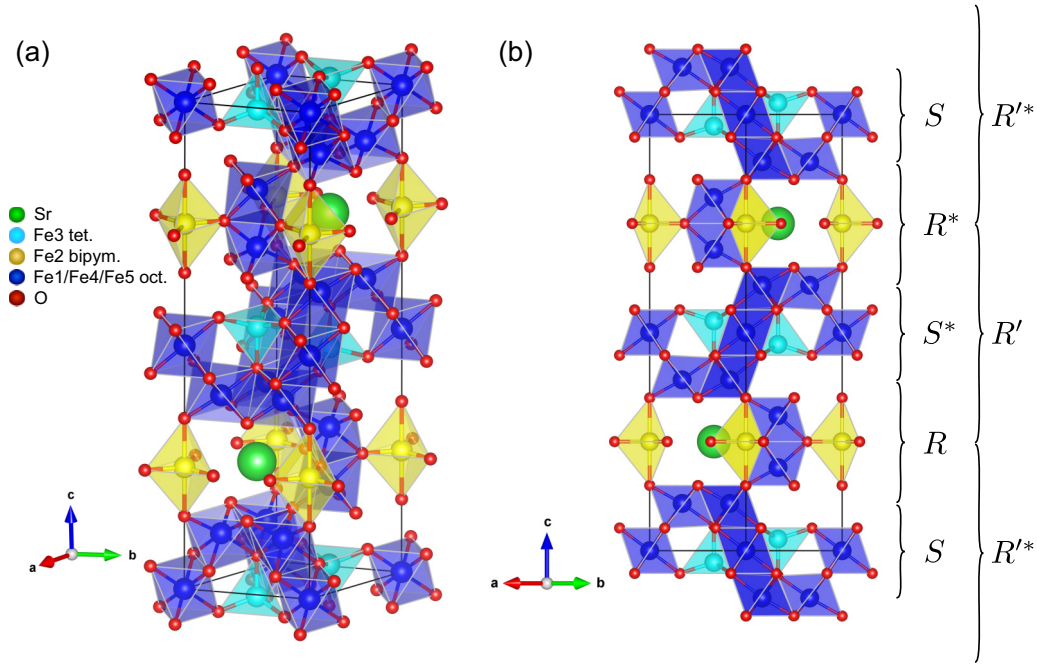

FIG. 1. (a) Perspective view of the hexagonal (space group $P6_3/mmc$) crystal structure of $SrSc_xFe_{12-x}O_{19}$ belonging to the family of M-hexaferrites that can be decomposed into R, S, R^*, and S^* blocks (b), where the asterisk denotes a π rotation around the c axis. The magnetic block R' (defined as R in Refs. [9,10]) extends between two layers of bipyramidally coordinated Fe, which is followed by R'^*.

Mössbauer studies of the $BaSc_{1.6}Fe_{10.4}O_{19}$ compound [10,11]. It was also found that Sc ions preferably occupy the octahedral positions $2a$, $4f2$, and $12k$ as compared to the tetrahedral $4f1$ and bipyramidal $2b$ sites (see Fig. 1) thus determining a specific variation of exchange interactions and magnetic anisotropy resulting in a decrease of spontaneous magnetization and a change in the magnetic structure. Recently, the magnetic and magnetoelectric properties of $BaSc_xFe_{12-x}O_{19}$ and $SrSc_xFe_{12-x}O_{19}$ ($x = 1.3$–1.7) hexaferrites have been studied [12,13], which has revealed the phase transitions from the high-temperature ferrimagnetic phase to the conical magnetic structure. Furthermore, even the Sr compounds possess a remarkable electric polarization that has not been reported before. The value of the magnetic-field-induced electric polarization exceeds 40 $\mu C/m^2$, being a record for M-type hexaferrites. Here we present a systematic powder neutron diffraction study on the Sr-based Sc-substituted M-hexaferrite compounds $SrSc_xFe_{12-x}O_{19}$ in order to elucidate the main features of their conical magnetic structures and how they might be related to their magnetoelectric properties.

II. EXPERIMENT

We have investigated Sr M-type hexaferrites using powder samples of three different compositions on the high-flux diffractometer D1B and on the high-resolution diffractometer D2B at the Institut Laue-Langevin (Grenoble, France). The samples were obtained by crushing an ingot containing several single-crystal blocks with different orientations. The ingot was synthesized by the crucibleless zone melting method with radiation (light) heating as described in Ref. [12]. We used ground polycrystalline samples with a mass of between 1.5 and 2.5 g, which were filled into vanadium sample containers with a diameter of 3 mm. A wavelength of 2.52 Å from the (002) reflection of the pyrolytic graphite monochromator was chosen for the D1B experiment, while a shorter wavelength of 1.59 Å from the (335) reflection of a Ge monochromator was preferred for the D2B experiment at room temperature in order to obtain structural information at high Q in the absence of magnetic scattering due to the magnetic form factor decay. On D1B each sample has been investigated using the following program: On cooling down to base temperature, diffraction patterns over a short acquisition time of 2 min were recorded that served to pinpoint the magnetic phase transition into the conical state for a more detailed investigation afterward. Consequently, diffraction patterns with a counting time of 4 times 30 min were recorded at base temperature and above the respective transition temperatures (between 100 and 200 K depending on the sample composition). Temperature ramps were carried out by recording diffraction patterns with an acquisition time of 2 min while ramping the temperature with a heating rate of +1 K/min. The transition temperature into the paramagnetic phase is well over room temperature, for which this transition could not be studied.

III. RESULTS AND DISCUSSION

A. High-resolution experiments

The high-resolution diffraction patterns covering a large Q range recorded at the D2B diffractometer were used to refine the nuclear and ferrimagnetic structure models at the same time. The fact that the magnetic form factor of the Fe^{3+} ion is below 0.1 for the high-angle region of the patterns allows a meaningful refinement of the nuclear structure. The refined structural parameters were the hexagonal lattice constants,

TABLE I. Refined lattice constants, atomic parameters, and temperature factors of the $SrSc_xFe_{12-x}O_{19}$ ($x = 1.4$, 1.6, and 1.8) nuclear structure investigation as well as the Fe magnetic moments along the c axis. The ferrimagnetic components are constrained to be $\mu_c(\text{Fe1}) = \mu_c(\text{Fe4}) = \mu_c(\text{Fe5})$ and $\mu_c(\text{Fe2}) = \mu_c(\text{Fe3})$. The respective Wyckoff sites are Sr $2d$ ($\frac{2}{3}$ $\frac{1}{3}$ $\frac{1}{4}$); Fe1/Sc1 $2a$ (0 0 0); Fe2/Sc2 $2b$ (0 0 $\frac{1}{4}$); Fe3/Sc3, Fe4/Sc4 and O2 $4f$ ($\frac{1}{3}$ $\frac{2}{3}$ z); Fe5/Sc5 and O4 $12k$ (x $2x$ z); O1 $4e$ (0 0 z); O3 $6h$ (x $2x$ $\frac{1}{4}$); O5 $24l$ (x y z) within the hexagonal space group $P6_3/mmc$.

	$x = 1.4$	$x = 1.6$	$x = 1.8$
a (Å)	5.9166(2)	5.9203(1)	5.9229(2)
c (Å)	23.348(1)	23.3798(5)	23.4097(8)
Fe3/Sc3 z	0.0267(3)	0.0262(2)	0.0252(3)
Fe4/Sc4 z	0.1886(3)	0.1881(2)	0.1864(3)
Fe5/Sc5 x	0.171(1)	0.1688(7)	0.1692(8)
Fe5/Sc5 z	0.8933(2)	0.8926(1)	0.8927(1)
O1 z	0.1494(5)	0.1480(4)	0.1485(4)
O2 z	0.9417(6)	0.9455(4)	0.9450(6)
O3 x	0.185(2)	0.184(1)	0.186(1)
O4 x	0.153(1)	0.1562(9)	0.156(1)
O4 z	0.0516(3)	0.0526(2)	0.0538(3)
O5 x	0.4988(5)	0.4978(3)	0.4994(5)
O5 y	0.010(2)	0.012(1)	0.010(2)
O5 z	0.149(3)	0.1486(2)	0.1493(2)
B_{iso}	0.10(4)	0.13(2)	0.09(3)
R_F (%)	12.5	7.0	8.2
$\mu_c(\text{Fe1})$ (μ_B)	2.5(1)	2.35(8)	2.1(1)
$\mu_c(\text{Fe2})$ (μ_B)	3.6(2)	3.5(2)	3.4(2)
R_F mag. (%)	13.1	10.7	11.8

the symmetry-constrained positions of all atoms, the occupation factor of Fe/Sc, and an overall isotropic temperature factor. A few parasitic peaks could be observed at lower diffraction angles, which consequently were excluded from the refinement. In view of the complex nuclear and magnetic structures due to five different magnetic sublattices, we have decided to limit the number of free parameters concerning the magnetic structure to a minimum. According to the reported preferential occupation of Sc ions, we have constrained the Fe magnetic moments among octahedral (Fe1, Fe4, and Fe5) and nonoctahedral sites (Fe2 and Fe3), which provides a satisfying result in terms of agreement factors. The results of the structural refinements are shown in Table I, and the diffraction pattern of the $x = 1.6$ sample is shown in Fig. 2.

It can be seen that the lattice constants increase with increasing Sc content due to the larger ionic radius of that atom in comparison to Fe. The atomic parameters are practically the same within the error bars for the three investigated compounds. The refinement of a single occupation factor implying the same ratio between Fe and Sc on each site returns the nominal concentration within the error bars. An attempt to refine the occupation factors on the respective Fe/Sc sites clearly suggests the preferential occupation of Sc on the octahedral sites, but results in the absence of Sc on the nonoctahedral sites and a higher overall Sc concentration, which, however, is still inside a 2σ interval. Therefore, we have deemed it more reasonable to identify the concentration x according to the transition temperatures from the ferrimagnetic to the conical phase given in Ref. [13], where the chemical compositions were verified by x-ray energy-dispersion analysis. Two of our three samples reveal that transition T^* at very similar temperatures (see Sec. III B), for which we identify those samples as $x = 1.4$ and 1.6. The third sample has a higher T^* than the samples investigated in Ref. [12]. However, following Vegard's rule, an increasing amount of the bigger Sc on the Fe site should result in increasing lattice constants, which is indeed confirmed by our results. We could therefore extrapolate the chemical composition that amounts to approximately $x = 1.8$. The ferrimagnetic structure was described using a single basis vector for all sites from the irreducible representation mGM2+ (Cracknell-Davies-Miller-Love notation [14]), which corresponds to the magnetic space group $P6_3mm'c'$. As expected, the magnetic moments show a decreasing trend with increasing content of nonmagnetic Sc. Due to the fact that Sc preferably occupies the octahedral sites, the reduction in the moment amplitude is more pronounced on those sites (16% reduction of μ_c for Fe1, Fe4, and Fe5 between $x = 1.4$ and 1.6) in comparison to the bipyramidally and tetrahedrally coordinated sites (6% reduction for Fe2 and Fe3), as can be seen in Table I. The ferrimagnetic structure consists of ferromagnetic Fe1-Fe2 chains with antiferromagnetically aligned Fe3-Fe4 chains. The magnetic moments on the Fe5 ions arranged on a triangle are parallel to the Fe1-Fe2 moments. The magnetic structure is visualized in Fig. 3(a). The worse agreement factors for the $x = 1.4$ sample are due to a higher volume fraction of parasitic peaks, which are not always isolated and therefore overlap with peaks of the main structure.

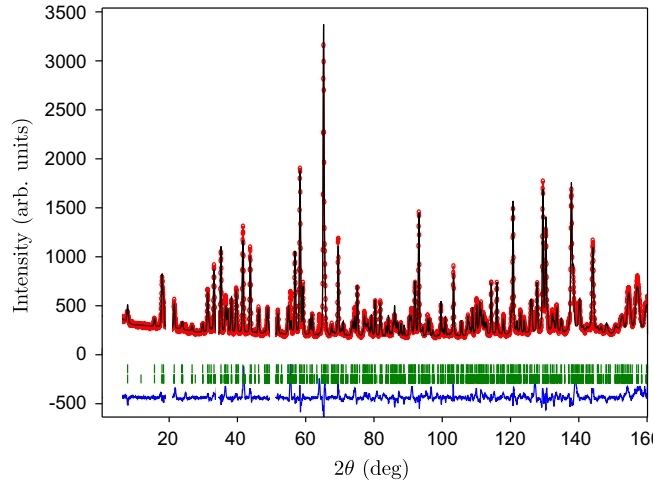

FIG. 2. Diffraction pattern of $SrSc_{1.6}Fe_{10.4}O_{19}$ taken at the high-resolution diffractometer D2B at room temperature. Red dots show the experimental data, the black solid line represents the calculated pattern, and the blue solid line at the bottom is the difference curve. Green vertical bars indicate the peak for the nuclear (first row) and magnetic Bragg peaks (second row).

B. High-flux experiments

The diffraction patterns recorded with a short acquisition time were used to construct thermodiffractograms, which are shown in Fig. 4. One can clearly observe the appearance of

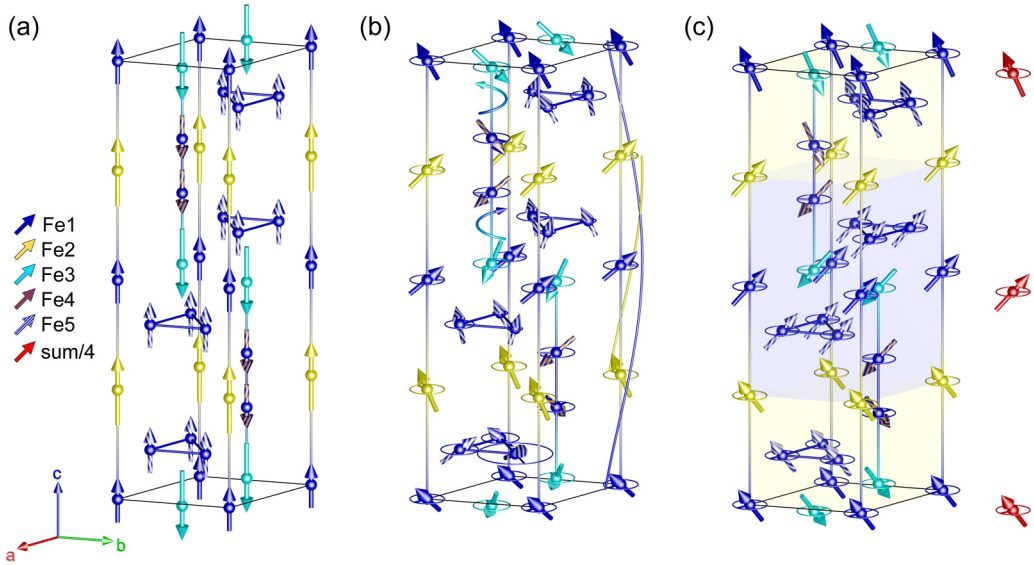

FIG. 3. Magnetic structures in the $SrSc_xFe_{12-x}O_{19}$ hexaferrites. According to the color code of Fig. 1, the octahedral sites are shown in dark blue while the bipyramidal and tetrahedral sites are shown in yellow and light blue, respectively. Magnetic moments among the octahedral sites are shown in plain blue for the $2a$ site, with orange stripes for the $4f$ site and with white stripes for the $12k$ site. Structural aspects like the Fe1-Fe2 and Fe3-Fe4 chains running along the c axis as well as the triangular configuration of Fe5 ions are emphasized by respective bonds. (a) Ferrimagnetic structure model refined from the high-resolution diffraction data at room temperature. (b) Conical magnetic structure model at 2 K derived from the high-flux diffraction data showing the superposition of the $\mathbf{q} = \mathbf{0}$ ferrimagnetic component and the $\mathbf{q} = (0\,0\,q_l)$ modulation of the in-plane component (shown by a circle with a horizontal bar indicating the in-plane moment direction). The antiphase rotation of Fe2 spins with respect to Fe1 spins is highlighted with spirals following the in-plane spin component in the direction of propagation. The antiphase rotation along the Fe3-Fe4-Fe4-Fe3 chain is symbolized by a left- or right-handed screw between the respective Fe3-Fe4 pairs. (c) Block-type magnetic structure with collinear spin alignment within R' and R'^* blocks (represented by yellow- and blue-shaded areas) as reported in Refs. [9,10]. The macrospin of each block is represented by a red arrow outside the unit cell and corresponds to $[\mu(\text{Fe1}) + \mu(\text{Fe2}) + 6\mu(\text{Fe5}) - 2\mu(\text{Fe3}) - 2\mu(\text{Fe4})]/4$.

satellite reflections at 2θ values of approximately 8°, 17°, and 20°. The positions of those reflections clearly shift as a function of temperature, indicating a temperature-dependent propagation vector. The satellite peaks could be indexed using a propagation vector $\mathbf{q} = (00q_l)$, where q_l lies between 0.67 and 0.8. Furthermore, it can be seen that the strongest reflection of the part of the diffraction pattern shown in Fig. 4 ($2\theta \approx 28°$) drops in intensity upon cooling. The Bragg peaks at 8° and 28° indexed as (002)-**q** and (100) and representing the in-plane modulation and the ferrimagnetic component, respectively, have been integrated at all temperatures. The integrated intensities and the position of the satellite expressed by the q_l value are shown in Fig. 5.

Vertical dashed lines indicate T^*, the onset of the satellite reflections, which happens to coincide with the onset of the decrease in the intensity of the main reflections, which therefore suggests a continuous spin reorientation down to low temperatures. Moreover, we find a good consistency with the magnetization maximum shown in Ref. [13]. The propagation vector seems to stay constant at an incommensurate value at low temperature for all investigated samples (Note that the low-temperature lattice constant obtained at $T = 2$ K on the high-flux diffractometer D1B was used to calculate the incommensurability q_l after having indexed the magnetic satellites.)

For the refinement of the low-temperature diffraction patterns, the nuclear structure was fixed to the results from the high-resolution data (Sec. III A), and the same constraints for the ferrimagnetic moments as described above were applied. To analyze the magnetic satellites, symmetry-adapted magnetic configurations were derived using the BASIREPS program. This yields six irreducible representations (four of dimension 1, two of dimension 2; see Table II), and the Fe3, Fe4, and Fe5 sites split into two orbits that are related by the twofold screw axis along $(xx0)$. Since the one-dimensional representations do not allow an in-plane component for sites other than $12k$, they were not useful to describe our experimental data. Furthermore, only one of the two two-dimensional representations (Γ_3) was able to explain the strong (002)-**q** reflection.

Given the complexity of the crystal and especially of the magnetic structures with split orbits and up to six basis vectors for the $12k$ site (e.g., ψ_3 with u_1, v_1, w_1, u_2, v_2, and w_2) and by judging what one might expect to extract from a powder dataset, we have considered the use of the fewest possible refinement parameters to be the most reasonable approach. The propagation vector of the form $(0\,0\,q_l)$ indicates frustrated interactions along the Fe1-Fe2 as well as the Fe3-Fe4 chains, which run along the c axis. We have therefore constrained the in-plane component of the magnetic moments to the same respective value along each of those chains (constraint 1 in Table III). Furthermore, we have used the same amplitude for the split sites (constraint 2 in Table III). Finally, when the use of two basis vectors was necessary (i.e., for the $12k$ site), their coefficients were constrained as well (constraint 3 in Table III). This leads to three refinable parameters describing

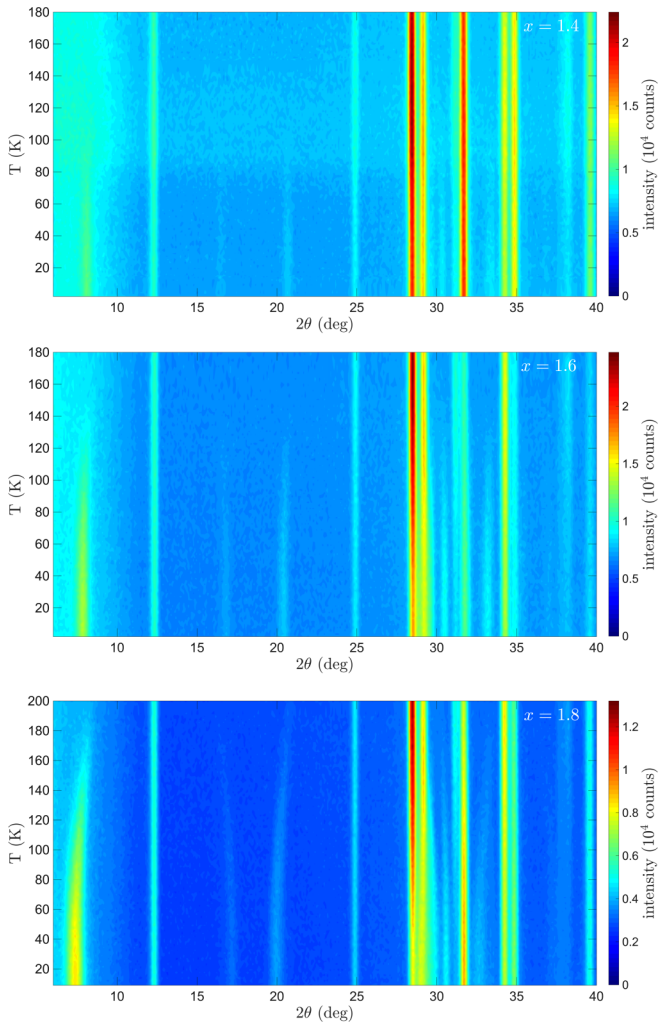

FIG. 4. Thermodiffraction patterns of $SrSc_xFe_{12-x}O_{19}$ for $x = 1.4$ (upper panel), $x = 1.6$ (central panel), and $x = 1.8$ (lower panel) showing the appearance of purely magnetic peaks and their shift as a function of temperature.

the sizes of the magnetic moments with an additional seven parameters that describe the phase of the respective modulation in relation to the first spin on the Fe1 ion. The magnetic mode within Γ_3 symmetry is therefore described by

$$\begin{aligned}\psi = {} & \psi'_{3,1}(u'_2 = C1) + \psi'_{3,2}(v'_2 = C1)e^{-2\pi i\varphi_2} \\ & + \psi'_{3,1}(u'_2 = C2)e^{-2\pi i\varphi_{3a}} + \psi'_{3,1}(u'_2 = C2)e^{-2\pi i\varphi_{3b}} \\ & + \psi'_{3,1}(u'_2 = C2)e^{-2\pi i\varphi_{4a}} + \psi'_{3,1}(u'_2 = C2)e^{-2\pi i\varphi_{4b}} \\ & + [\psi_{3,1}(u_1 = C3) + \psi_{3,2}(u_2 = C3)]e^{-2\pi i\varphi_{5a}} \\ & + [\psi_{3,1}(u_1 = C3) + \psi_{3,2}(u_2 = C3)]e^{-2\pi i\varphi_{5b}}, \end{aligned} \quad (1)$$

where the coefficients C_n and phases φ_n are the refinable parameters, and a and b denote the split sites. The magnetic structure factor is then given by

$$\mathbf{M}(\mathbf{Q}) = \sum_j \mathbf{S}^{\Gamma_n}_{\mathbf{q},j} f_j(\mathbf{Q}) T_j \exp(-i\mathbf{Q}\mathbf{r}_j), \quad (2)$$

where the sum goes over all atoms j of the unit cell, $\mathbf{Q}$ is the scattering vector, f_j is the magnetic form factor, T_j is the

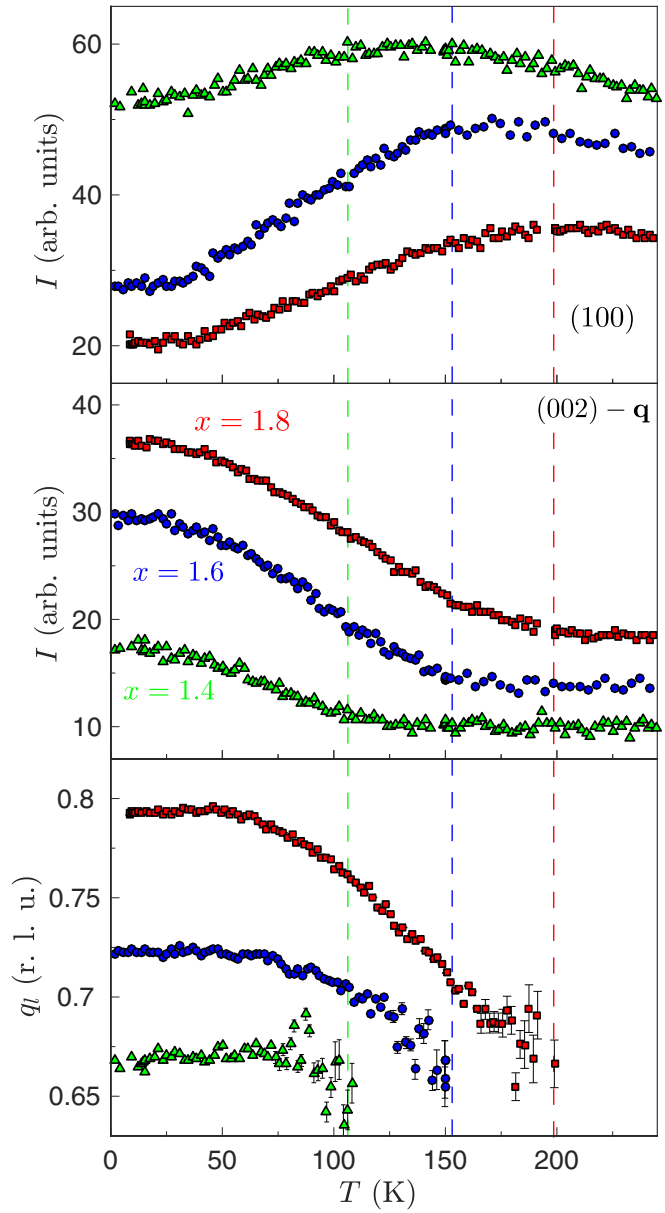

FIG. 5. Integrated intensities of the nuclear/ferrimagnetic (100) reflection (upper panel) and the purely magnetic satellite (002)-**q** (central panel) as well as the incommensurability q_l of the latter (lower panel) as a function of temperature for $SrSc_xFe_{12-x}O_{19}$ with $x = 1.4$, 1.6, and 1.8. Vertical dashed lines indicate the transition from the ferrimagnetic to the conical phase. The curves in the upper and central panel are shifted vertically for clarity.

Debye-Waller factor, and $\mathbf{r}_j$ is the position vector of atom j. $\mathbf{S}^{\Gamma_n}_{\mathbf{q},j}$ is the Fourier coefficient of the magnetic moment of atom j connected to the propagation vector $\mathbf{q}$, which consists of the linear combination of basis vectors within the symmetry of Γ_n of the associated site. Following the decomposition of the magnetic mode in Eq. (1), the Fourier coefficients of, e.g., Fe1 and Fe5a would be $\mathbf{S}^{\Gamma_3}_{\mathbf{q},1} = \psi'_{3,1}(u'_2 = C1)$ and $\mathbf{S}^{\Gamma_3}_{\mathbf{q},5a} = [\psi_{3,1}(u_1 = C3) + \psi_{3,2}(u_2 = C3)]e^{-2\pi i\varphi_{5a}}$, respectively, while the Fourier coefficients of the symmetry-related sites are summed after transforming the spin

TABLE II. Basis vectors ψ_n of the irreducible representations Γ_n for each of the split magnetic sites $12k$ at given fractional coordinates (x, y, z) associated with a propagation vector $\mathbf{q} = (0, 0, q_l)$. The phase shift corresponding to the twofold screw axis 2_z is $a = \exp(-i\pi q_l)$. Note that the basis vectors ψ'_n of the remaining sites can be derived from the more general site $12k$ and are $\psi'_1 = 0$, $\psi'_2 = \psi_2(u = 0, w = w')$, $\psi'_{3,1} = i[\psi_{3,2}(v_2 = w_2 = 0, u_2 = u'_2) - \psi_{3,1}(u_1 = w_1 = 0, v_1 = u'_2)]$, $\psi'_{3,2} = -i[\psi_{3,2}(u_2 = w_2 = 0, v_2 = v'_2) + \psi_{3,2}(v_2 = w_2 = 0, u_2 = v'_2) + \psi_{3,1}(v_1 = w_1 = 0, u_1 = v'_2)]$, $\psi'_4 = 0$, $\psi'_5 = \psi_5(u = 0, w = w')$, $\psi'_{6,1} = i[\psi_{6,2}(v_2 = w_2 = 0, u_2 = u'_2) - \psi_{6,1}(u_1 = w_1 = 0, v_1 = u'_2)]$ and $\psi'_{6,2} = -i[\psi_{6,2}(u_2 = w_2 = 0, v_2 = v'_2) + \psi_{6,2}(v_2 = w_2 = 0, u_2 = v'_2) + \psi_{6,1}(v_1 = w_1 = 0, u_1 = v'_2)]$ due to the higher site symmetry. The second index m in the basis vectors of two-dimensional representations $\psi_{n,m}$ denotes the dimension to which the basis vectors refer and are shown in the mth row of the corresponding ψ_n. The components u, v, and w connected to the Fourier coefficients $\mathbf{S}^{\Gamma_n}$ of each atomic position have been refined according to their constraints (an overline indicates a negative number). All components u, v, and w may be complex.

	$\begin{pmatrix} x \\ y \\ z \end{pmatrix}$	$\begin{pmatrix} \overline{x} \\ \overline{y} \\ z + 1/2 \end{pmatrix}$	$\begin{pmatrix} \overline{y} \\ x - y \\ z \end{pmatrix}$	$\begin{pmatrix} y \\ \overline{x} + y \\ z + 1/2 \end{pmatrix}$	$\begin{pmatrix} \overline{x} + y \\ \overline{x} \\ z \end{pmatrix}$	$\begin{pmatrix} x - y \\ x \\ z + 1/2 \end{pmatrix}$
ψ_1	$\begin{pmatrix} u \\ 0 \\ 0 \end{pmatrix}$	$a\begin{pmatrix} \overline{u} \\ 0 \\ 0 \end{pmatrix}$	$\begin{pmatrix} 0 \\ u \\ 0 \end{pmatrix}$	$a\begin{pmatrix} 0 \\ \overline{u} \\ 0 \end{pmatrix}$	$\begin{pmatrix} \overline{u} \\ \overline{u} \\ 0 \end{pmatrix}$	$a\begin{pmatrix} u \\ u \\ 0 \end{pmatrix}$
ψ_2	$\begin{pmatrix} u \\ 2u \\ w \end{pmatrix}$	$a\begin{pmatrix} \overline{u} \\ 2\overline{u} \\ w \end{pmatrix}$	$\begin{pmatrix} 2\overline{u} \\ \overline{u} \\ w \end{pmatrix}$	$a\begin{pmatrix} 2u \\ u \\ w \end{pmatrix}$	$\begin{pmatrix} u \\ \overline{u} \\ w \end{pmatrix}$	$a\begin{pmatrix} \overline{u} \\ u \\ w \end{pmatrix}$
ψ_3	$\begin{pmatrix} u_1 \\ v_1 \\ w_1 \end{pmatrix}$	$a\begin{pmatrix} \overline{u}_1 \\ \overline{v}_1 \\ w_1 \end{pmatrix}$	$\frac{1}{2}\begin{pmatrix} v_1 - i\sqrt{3}v_1 \\ (\overline{u}_1 + v_1)(1 - i\sqrt{3}) \\ \overline{w}_1 - i\sqrt{3}\overline{w}_1 \end{pmatrix}$	$\frac{1}{2}a\begin{pmatrix} \overline{v}_1 - i\sqrt{3}\overline{v}_1 \\ (u_1 + \overline{v}_1)(1 - i\sqrt{3}) \\ \overline{w}_1 - i\sqrt{3}\overline{w}_1 \end{pmatrix}$	$\frac{1}{2}\begin{pmatrix} (u_1 + \overline{v}_1)(1 + i\sqrt{3}) \\ u_1 - i\sqrt{3}\overline{u}_1 \\ \overline{w}_1 - i\sqrt{3}w_1 \end{pmatrix}$	$\frac{1}{2}a\begin{pmatrix} (\overline{u}_1 + v_1)(1 + i\sqrt{3}) \\ \overline{u}_1 - i\sqrt{3}u_1 \\ \overline{w}_1 - i\sqrt{3}w_1 \end{pmatrix}$
	$\frac{1}{2}\begin{pmatrix} (\overline{u}_2 + v_2)(1 - i\sqrt{3}) \\ v_2 - i\sqrt{3}v_2 \\ w_2 - i\sqrt{3}w_2 \end{pmatrix}$	$\frac{1}{2}a\begin{pmatrix} (u_2 + \overline{v}_2)(1 - i\sqrt{3}) \\ \overline{v}_2 - i\sqrt{3}\overline{v}_2 \\ w_2 - i\sqrt{3}w_2 \end{pmatrix}$	$\begin{pmatrix} v_2 \\ u_2 \\ \overline{w}_2 \end{pmatrix}$	$a\begin{pmatrix} \overline{v}_2 \\ \overline{u}_2 \\ \overline{w}_2 \end{pmatrix}$	$\frac{1}{2}\begin{pmatrix} u_2 - i\sqrt{3}\overline{u}_2 \\ (u_2 + \overline{v}_2)(1 + i\sqrt{3}) \\ w_2 - i\sqrt{3}\overline{w}_2 \end{pmatrix}$	$\frac{1}{2}a\begin{pmatrix} \overline{u}_2 - i\sqrt{3}u_2 \\ (\overline{u}_2 + v_2)(1 + i\sqrt{3}) \\ w_2 - i\sqrt{3}\overline{w}_2 \end{pmatrix}$
ψ_4	$\begin{pmatrix} u \\ 0 \\ 0 \end{pmatrix}$	$a\begin{pmatrix} u \\ 0 \\ 0 \end{pmatrix}$	$\begin{pmatrix} 0 \\ u \\ 0 \end{pmatrix}$	$a\begin{pmatrix} 0 \\ u \\ 0 \end{pmatrix}$	$\begin{pmatrix} \overline{u} \\ \overline{u} \\ 0 \end{pmatrix}$	$a\begin{pmatrix} \overline{u} \\ \overline{u} \\ 0 \end{pmatrix}$
ψ_5	$\begin{pmatrix} u \\ 2u \\ w \end{pmatrix}$	$a\begin{pmatrix} u \\ 2u \\ \overline{w} \end{pmatrix}$	$\begin{pmatrix} 2\overline{u} \\ \overline{u} \\ w \end{pmatrix}$	$a\begin{pmatrix} 2\overline{u} \\ \overline{u} \\ \overline{w} \end{pmatrix}$	$\begin{pmatrix} u \\ \overline{u} \\ w \end{pmatrix}$	$a\begin{pmatrix} u \\ \overline{u} \\ \overline{w} \end{pmatrix}$
ψ_6	$\begin{pmatrix} u_1 \\ v_1 \\ w_1 \end{pmatrix}$	$a\begin{pmatrix} u_1 \\ v_1 \\ \overline{w}_1 \end{pmatrix}$	$\frac{1}{2}\begin{pmatrix} v_1 - i\sqrt{3}v_1 \\ (\overline{u}_1 + v_1)(1 - i\sqrt{3}) \\ \overline{w}_1 - i\sqrt{3}\overline{w}_1 \end{pmatrix}$	$\frac{1}{2}a\begin{pmatrix} v_1 - i\sqrt{3}v_1 \\ (\overline{u}_1 + v_1)(1 - i\sqrt{3}) \\ w_1 - i\sqrt{3}w_1 \end{pmatrix}$	$\frac{1}{2}\begin{pmatrix} (u_1 + \overline{v}_1)(1 + i\sqrt{3}) \\ u_1 - i\sqrt{3}\overline{u}_1 \\ \overline{w}_1 - i\sqrt{3}w_1 \end{pmatrix}$	$\frac{1}{2}\begin{pmatrix} (u_1 + \overline{v}_1)(1 + i\sqrt{3}) \\ u_1 - i\sqrt{3}\overline{u}_1 \\ w_1 - i\sqrt{3}\overline{w}_1 \end{pmatrix}$
	$\frac{1}{2}\begin{pmatrix} (\overline{u}_2 + v_2)(1 - i\sqrt{3}) \\ v_2 - i\sqrt{3}v_2 \\ w_2 - i\sqrt{3}w_2 \end{pmatrix}$	$\frac{1}{2}a\begin{pmatrix} (\overline{u}_2 + v_2)(1 - i\sqrt{3}) \\ v_2 - i\sqrt{3}v_2 \\ \overline{w}_2 - i\sqrt{3}\overline{w}_2 \end{pmatrix}$	$\begin{pmatrix} v_2 \\ u_2 \\ \overline{w}_2 \end{pmatrix}$	$a\begin{pmatrix} v_2 \\ u_2 \\ w_2 \end{pmatrix}$	$\frac{1}{2}\begin{pmatrix} u_2 - i\sqrt{3}\overline{u}_2 \\ (u_2 + \overline{v}_2)(1 + i\sqrt{3}) \\ w_2 - i\sqrt{3}\overline{w}_2 \end{pmatrix}$	$\frac{1}{2}a\begin{pmatrix} u_2 - i\sqrt{3}\overline{u}_2 \\ (u_2 + \overline{v}_2)(1 + i\sqrt{3}) \\ \overline{w}_2 - i\sqrt{3}w_2 \end{pmatrix}$

TABLE III. Constraints and coefficients used to refine the complex modulated in-plane components of the conical magnetic structure.

Number	Coefficient	Constrained parameters
1	$C1$	$\mu(\text{Fe1})_{ab} = \mu(\text{Fe2})_{ab}$ $\mu(\text{Fe3})_{ab} = \mu(\text{Fe4})_{ab}$
2	$C2$	$\mu(\text{Fe3}a)_{ab} = \mu(\text{Fe3}b)_{ab}$ $\mu(\text{Fe4}a)_{ab} = \mu(\text{Fe4}b)_{ab}$ $\mu(\text{Fe5}a)_{ab} = \mu(\text{Fe5}b)_{ab}$
3	$C3$	$\mu(\text{Fe5})_{\psi_{3,1}} = \mu(\text{Fe5})_{\psi_{3,2}}$
4		$\varphi_{3b} - \varphi_{3a} = q_l$ $\varphi_{4b} - \varphi_{4a} = q_l - 1$ $\varphi_{5b} - \varphi_{5a} = 1 - q_l$

components and the position according to the symmetry operators of the magnetic subgroup. The magnetic moment of site j ($\mathbf{m}_j$) in the unit cell L (position vector $\mathbf{R}_L$) can be written as

$$\mathbf{m}_j(\mathbf{R}_L) = \frac{1}{2}\sum_{\mathbf{q}} \mathbf{S}^{\Gamma_n}_{\mathbf{q},j} \exp(i\mathbf{q}\mathbf{R}_L) + \mathbf{S}^{\Gamma^*_n}_{\mathbf{q},j} \exp(-i\mathbf{q}\mathbf{R}_L), \quad (3)$$

where the star symbol denotes complex conjugation. The approach of limiting the varying parameters led to a reasonably good refinement, which confirms the correct choice of representations. A comparison of this preliminary result with the magnetic superspace symmetry, which can be obtained by the program ISODISTORT [15], suggests the irreducible representation mDT5 (Cracknell-Davies-Miller-Love notation [14]) with the distortion mode 4D, which corresponds to the magnetic space group $P2_11'$. The use of the superspace symmetry fixes the phases between the split sites, therefore reducing the number of refinable parameters by 3 (constraint 4 in Table III). Our refinement, therefore, takes into account seven parameters in total, and the distinctly best results are shown in Table IV, whereas the resulting calculated diffraction patterns are depicted in Fig. 6. The proposed conical magnetic structure is shown in Fig. 3(b) in comparison to the block-type magnetic structure in Fig. 3(c).

To compare the magnetic structures among the different compositions in the most reasonable way, especially regarding the cone opening angles, we have used exactly the same combination of basis vectors for all datasets. Due to the lower quality of the data for $x = 1.8$ and especially $x = 1.4$, the agreement factors for the in-plane modulated component are considerably worse, however the evolution of the conical magnetic structure as a function of Sc doping is significant: We observe a striking reduction of the axial ferrimagnetic moment with increasing Sc doping in favor of a strong in-plane component. This can be evidenced by following the (100) and (101) reflections containing the axial ferrimagnetic contribution as well as the (002)-**q** satellite as a function of Sr doping, which clearly reveals a proportional increase of the in-plane component and therefore the opening of the cone angle (Fig. 7). Furthermore, the q_l value of the propagation vector shows a clear dependence on the Sc content revealing a longer pitch for higher x.

TABLE IV. Refined parameters for the description of the axial (μ_c) and in-plane (μ_{ab}) components in the low-temperature conical phase of $SrSc_xFe_{12-x}O_{19}$ ($x = 1.4$, 1.6, and 1.8). The ferrimagnetic components are restricted as for the room-temperature refinement, i.e., $\mu_c(\text{Fe1}) = \mu_c(\text{Fe}w4) = \mu_c(\text{Fe5})$ and $\mu_c(\text{Fe2}) = \mu_c(\text{Fe3})$. The irreducible representation mDT5 with the distortion mode 4D (corresponding to the magnetic space group $P2_11'$) was employed for the in-plane modulation, which is described by the parameters C_n and the phases φ_n according to Eq. (1). The magnitude of the in-plane component is given by μ_{ab}, where $\mu_{ab}(\text{Fe1}) = \mu_{ab}(\text{Fe2}) = 2/\sqrt{3}C_1$, $\mu_{ab}(\text{Fe3}) = \mu_{ab}(\text{Fe4}) = 2/\sqrt{3}C_2$, and $\mu_{ab}(\text{Fe5}) = C_5$. α denotes half of the cone opening defined as $\tan^{-1}(\mu_{ab}/\mu_c)$.

	$x = 1.4$	$x = 1.6$	$x = 1.8$
q_l (r.l.u.)	0.668(2)	0.725(1)	0.793(1)
μ_c(Fe1) (μ_B)	2.4(2)	2.26(8)	1.7(1)
μ_c(Fe2) (μ_B)	3.7(1)	2.7(1)	1.5(3)
R_F mag. c (%)	10.2	9.2	9.5
C_1 (μ_B)	1.6(8)	2.9(5)	4.7(4)
C_2 (μ_B)	3.1(5)	3.1(3)	3.3(3)
C_3 (μ_B)	2.5(4)	2.9(2)	3.3(3)
φ_2	0.3(2)	0.62(7)	0.61(7)
φ_{3a}	0.5(1)	0.67(5)	0.36(3)
φ_{4a}	0.3(1)	0.54(7)	0.36(5)
φ_{5a}	0.5(1)	0.84(6)	0.53(5)
μ_{ab}(Fe1) (μ_B)	1.4(7)	2.5(4)	4.1(4)
μ_{ab}(Fe3) (μ_B)	2.6(5)	2.7(3)	2.9(3)
μ_{ab}(Fe5) (μ_B)	2.5(4)	2.9(2)	3.3(2)
α(Fe1) (deg)	30(13)	48(5)	68(2)
α(Fe2) (deg)	21(9)	43(5)	70(4)
α(Fe3) (deg)	35(5)	45(3)	63(5)
α(Fe4) (deg)	47(6)	50(3)	60(3)
α(Fe5) (deg)	46(5)	52(2)	63(2)
R_F mag. ab (%)	28.6	17.9	24.2

IV. DISCUSSION

We have presented a powder neutron diffraction study combining high-resolution and high-flux experiments on the $SrSc_xFe_{12-x}O_{19}$ hexaferrites with $x = 1.4$, 1.6, and 1.8, which revealed the nature of the different magnetic structures. Due to the fact that the paramagnetic phase lies well above room temperature, our high-resolution data extending to reasonably large Q values were necessary to analyze the nuclear and the ferrimagnetic structure simultaneously. The magnetic structure model above T^* is in agreement with the one proposed in Ref. [9] for the undoped compound. Here, on the contrary, we can rule out a canting of the spins away from the c axis in the high-temperature ferrimagnetic phase. At low temperature we revealed a helicoidal modulation of the in-plane components on the Fe1-Fe2 and Fe3-Fe4 chains that, together with the ferrimagnetic component, results in a conical structure. A triangular spin configuration with a nonzero net magnetic moment in the plane was found for the Fe5 triangle structure motif, which is sinusoidally modulated from triangle to triangle. However, it has to be stated that different phases on the Fe3-Fe4 chain and different triangular configurations (from other combinations of basis vectors) on the Fe5 sites lead to slightly worse agreement factors. Such details can only be unambiguously derived using single-crystal samples.

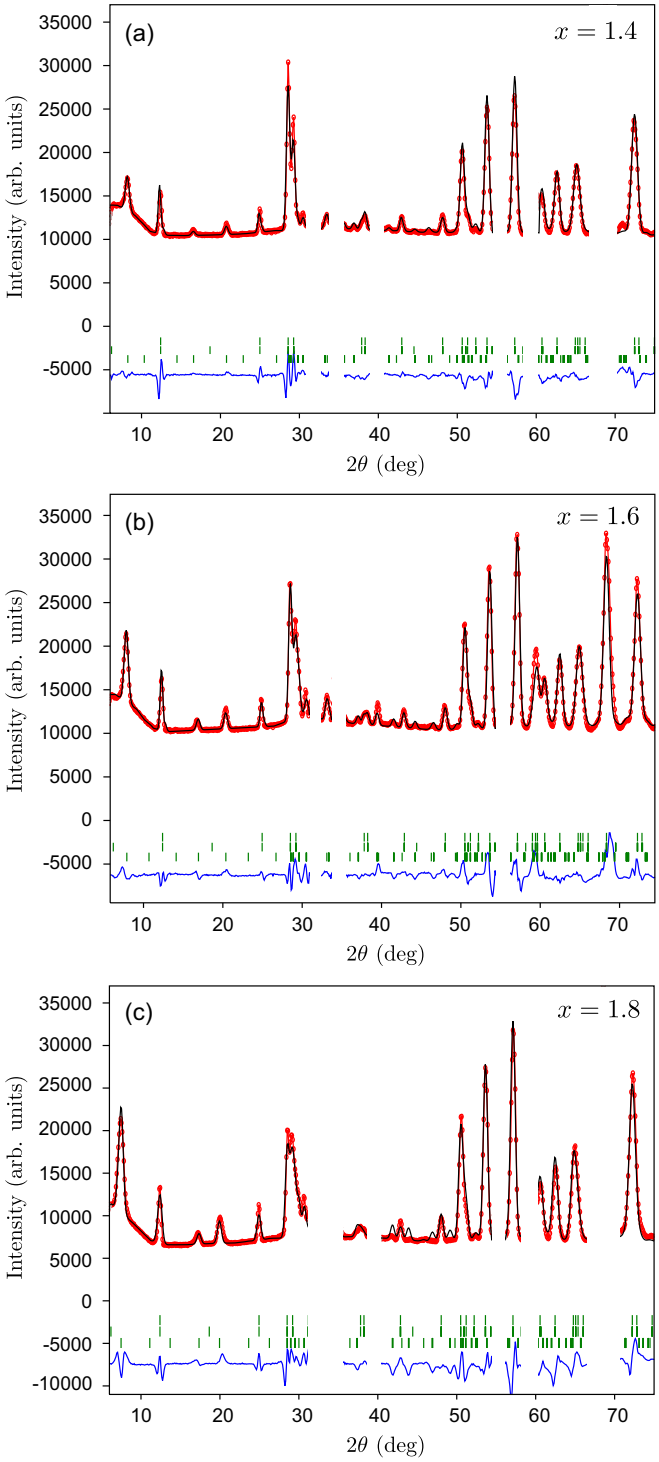

FIG. 6. Diffraction patterns of $SrSc_xFe_{1-x}O_{19}$ taken at the high-flux diffractometer D1B at $T = 2$ K for (a) $x = 1.4$, (b) $x = 1.6$, and (c) $x = 1.8$. Red dots show the experimental data, the black solid line represents the calculated pattern, and the blue solid line at the bottom is the difference curve. Green vertical bars indicate the peak for the nuclear (first row), magnetic $\mathbf{q} = \mathbf{0}$ Bragg peaks (second row), and magnetic $\mathbf{q} = (0\,0\,q_l)$ Bragg peaks (third row).

The magnetic satellites can only be explained by one of the six irreducible representations, however the resulting spin configuration differs substantially from the simple block-type magnetic structure [9,10]. In fact, by testing the latter on our

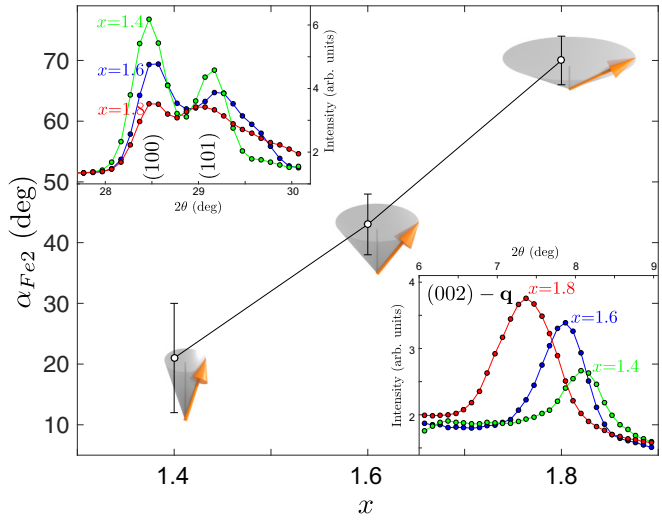

FIG. 7. Representative half-cone-opening angle of the Fe2 spin as a function of Sc doping x. It can clearly be observed how the in-plane component [lower right inset showing the (002)-**q** satellite] increases proportionally with respect to the axial ferrimagnetic component [upper left inset focusing on the (100) and (101) reflections]. The respective intensities are normalized with respect to the refined scale factor. The resulting cones are sketched for every composition.

data, we obtain $R_F = 26.5$ compared to our best fit for the $x = 1.6$ sample, which yielded $R_F = 17.9$. A clear improvement can be observed when subsequently adding more degrees of freedom to the block-type structure, e.g., a refinable phase for each site ($R_F = 23.0$) or noncollinear basis vectors for the triangular Fe5 site ($R_F = 21.5$), which applied together yield our proposed magnetic structure. Most importantly, we want to point out that the block-type magnetic structure cannot be explained within either irreducible representation of $P6_3/mmc$, since it would require the same basis vector for all sites. It is allowed, in principle, to use one basis vector $\psi'_{3,1}$, since for site $12k$ it can be decomposed into

$$\psi'_{3,1} = \psi_{3,1}(v_1 = w_1 = 0) - \frac{i}{\sqrt{3}}\psi_{3,1}(v_1 = w_1 = 0) - \frac{2i}{\sqrt{3}}\psi_{3,1}(u_1 = w_1 = 0), \quad (4)$$

but it is not possible to achieve a collinear configuration on a triangular plaquette due to the 3^+ rotation axis connecting Fe5 spins on positions (x y z) and ($\bar{y}$ x-y z), which would require a further symmetry breaking. The transition from the ferrimagnetic structure to the low-temperature conical phase is effectuated by a continuous opening of the cone angle below T^*, which can be derived from the monotonic increase and decrease of the magnetic satellite peak and integer peak intensity, respectively (Fig. 5). The nonmagnetic Sc on the Fe sites has a huge impact on the cone angles increasing from $\alpha = 36°$ ($x = 1.4$) to 48° ($x = 1.6$) and 65° ($x = 1.8$) averaged over all Fe sites at $T = 2$ K (see Table IV). In fact, the doping impact on the cone opening is most pronounced along the Fe1-Fe2 chain (see Table IV). Such a significant change is probably connected with a continuous transition from an easy-axis to an easy-plane anisotropy with decreasing temperature

and increasing Sc content. The cone angles reported here are slightly bigger than in the Ba M-type hexaferrite [10], which agrees with the higher electric polarization value.

V. CONCLUSION

Concerning the modulation of the different magnetic structures, our thermodiffraction patterns clearly reveal a temperature-dependent propagation vector that shows the same tendency as in Ref. [10]. Moreover, a pronounced difference in the pitch of the magnetic structures is present for the different compounds, with magnetic unit cells being ≈3 and ≈5 times larger than the nuclear ones for $x = 1.4$ and 1.8, respectively. An incommensurability along the c^* direction can only originate from competing interactions along the Fe1-Fe2 and Fe3-Fe4 chains. In the oversimplified case of a single helical chain, those interactions determine the incommensurate propagation vector of the magnetic structures according to $\cos(q_l\pi) \approx -J_{nn}/4J_{nnn}$ (Refs. [16–18]). A larger q_l value would therefore indicate a proportionally increasing nearest-neighbor interaction (J_{nn}). However, the scenario in the hexaferrite compound is by far more complicated, and the fact that the transition temperature T^* increases with increasing Sc doping (in agreement with the phase diagrams reported in Ref. [13]) speaks in favor of a higher degree of frustration. It has indeed been observed in $SrCr_8Ga_4O_{19}$ that nonmagnetic defects can disconnect the magnetic sublattices and even completely prevent long-range order [19]. Our detailed symmetry analysis suggests that at least for the Sr-based M-hexaferrites, the true magnetic structure is far more complex than previously assumed, since the simple block-type model is not compatible with our data. In particular, the collinear Fe5 spin alignment on the triangular structure motif is questionable. However, given the complexity of the proposed magnetic structure, it is difficult to reconcile the structural details with the macroscopic electric polarization. The approach of explaining the electric polarization by the inverse Dzyaloshinskii-Moriya effect is purely qualitative and does not account for the internal magnetic structure of the blocks composed of different sublattices. To explain the fact that the field dependence of polarization for Y-type hexaferrites is odd, while for Z-type it is even and for M-type it may be of both kinds, one has to make additional assumptions concerning the different types of domain boundaries [10,12,13]. It is shown in our work that conical magnetic structures in M-type Sr-Sc hexaferrites do exist for certain Sc concentrations. However, the real structure is more complex than the block model suggests: each iron spin of a different sublattice has its specific cone angle, therefore having its own contribution to the electric polarization. To quantitatively calculate the polarization and to make any conclusions about the specifics of the magnetoelectric coupling in different types of hexaferrites revealing different magnetic structures is even more difficult than for their simplified (block) models and has not been achieved yet (note that Y- and Z-type hexaferrites contain additional structural blocks and reveal transverse conical magnetic structures with the ferrimagnetic moment and electric polarization in the basal plane). The electric polarization can therefore only be determined by a number of microscopic parameters and specific fine features of the magnetic structure, which, however, require a special analysis that is beyond the scope of the present work. In addition, the experimentally observed polarization is often determined by other factors, especially by the electrical conductivity, which limits the value of the voltage applied during the preliminary poling of the samples. Bearing this in mind, it is hardly possible to draw conclusions concerning significant differences between Ba and Sr hexaferrites. Nevertheless, we suggest that the decisive factor responsible for the higher polarization observed in Sr hexaferrites with respect to the Ba compounds is their lower transition temperature into the conical structure, allowing a more efficient poling due to the reduced conductivity. Comparing the macroscopic properties with the microscopic magnetic structure, it becomes obvious that the magnitude of the electric polarization goes along with the opening of the cone angle, which is an intrinsic property and increases with increasing Sc concentration. In fact, the highest polarization values for both Ba and Sr hexaferrites were observed for $x = 1.6$. However, a further increase of doping does not result in a higher electric polarization due to the increasing T^*, thus preventing an efficient poling of the sample because of its higher electrical conductivity as an extrinsic factor. Although we report the cone opening angle to be slightly higher than in the Ba compounds, which goes along with the higher electric polarization, it is not certain that it is conserved when a transverse magnetic field is applied, which tilts the whole cone and induces the multiferroic state. Future single-crystal experiments will therefore hopefully shed more light on this highly complex system.

ACKNOWLEDGMENTS

This paper was supported by the Russian Scientific Foundation (Project No. 16-12-10531). Financial support from the Spanish Ministry of Economy, Competitiveness and Universities, through Projects No. MAT2014-56063-C2-1-R and No. MAT2017-85232-R (AEI/FEDER, EU), is acknowledged. We acknowledge ILL and D1B-CRG Ministerio de Economía y Competitividad (MINECO) for beam time allocation.

[1] T. Kimura, G. Lawes, and A. P. Ramirez, Phys. Rev. Lett. **94**, 137201 (2005).

[2] S. Ishiwata, Y. Taguchi, H. Murakawa, Y. Onose, and Y. Tokura, Science **319**, 1643 (2008).

[3] Y. Kitagawa, Y. Hiraoka, T. Honda, T. Ishikura, H. Nakamura, and T. Kimura, Nat. Mater. **9**, 797 (2010).

[4] M. Soda, T. Ishikura, H. Nakamura, Y. Wakabayashi, and T. Kimura, Phys. Rev. Lett. **106**, 087201 (2011).

[5] S. H. Chun, Y. S. Chai, B.-G. Jeon, H. J. Kim, Y. S. Oh, I. Kim, H. Kim, B. J. Jeon, S. Y. Haam, J.-Y. Park *et al.*, Phys. Rev. Lett. **108**, 177201 (2012).

[6] K. Okumura, T. Ishikura, M. Soda, T. Asaka, H. Nakamura, Y. Wakabayashi, and T. Kimura, Appl. Phys. Lett. **98**, 212504 (2011).

[7] S. H. Chun, Y. S. Chai, Y. S. Oh, D. Jaiswal-Nagar, S. Y. Haam, I. Kim, B. Lee, D. H. Nam, K.-T. Ko, J.-H. Park *et al.*, Phys. Rev. Lett. **104**, 037204 (2010).

[8] R. C. Pullar, Prog. Mater. Sci. **57**, 1191 (2012).

[9] O. P. Aleshko-Ozhevskiĭ, R. A. Sizov, I. I. Yamzin, and V. A. Lubimtsev, Sov. Phys.: J. Exp. Theor. Phys. **28**, 425 (1969).

[10] Y. Tokunaga, Y. Kaneko, D. Okuyama, S. Ishiwata, T. Arima, S. Wakimoto, K. Kakurai, Y. Taguchi, and Y. Tokura, Phys. Rev. Lett. **105**, 257201 (2010).

[11] Z. Somogyvári, E. Sváb, K. Krezhov, L. F. Kiss, D. Kaptás, I. Vincze, E. Beregi, and F. Bourèe, J. Magn. Magn. Mater. **304**, e775 (2006).

[12] A. M. Balbashov, V. Yu. Ivanov, A. A. Mukhin, L. D. Iskhakova, Y. F. Popov, G. P. Vorob'ev, and M. E. Voronchikhina, JETP Lett. **101**, 489 (2015).

[13] V. Yu. Ivanov, A. M. Balbashov, A. A. Mukhin, L. D. Iskhakova, and M. E. Voronchikhina, JETP **124**, 604 (2017).

[14] A. P. Cracknell, B. L. Davies, S. C. Miller, and W. F. Love, *General Introduction and Tables of Irreducible Representation of Space Groups* (IFI/Plenum, New York, 1979).

[15] H. T. Stokes, D. M. Hatch, and B. J. Campbell, Isotropy, stokes.byu.edu/isotropy.html.

[16] M. Kenzelmann, A. B. Harris, A. Aharony, O. Entin-Wohlman, T. Yildirim, Q. Huang, S. Park, G. Lawes, C. Broholm, N. Rogado *et al.*, Phys. Rev. B **74**, 014429 (2006).

[17] T. A. Kaplan, Phys. Rev. **124**, 329 (1961).

[18] T. Nagamiya, in *Solid State Physics*, edited by F. Seitz and D. Turnbull (Academic, New York, 1967), Vol. 29, p. 346.

[19] X. Obradors, A. Labarta, A. Isalgué, J. Tejada, J. Rodriguez, and M. Pernet, Solid State Commun. **65**, 189 (1988).